Solid State Sciences 136 (2023) 107107

Contents lists available at ScienceDirect

Solid State Sciences

journal homepage: www.elsevier.com/locate/ssscie

Microstructural and magneto-optical properties of $Co_{1-x}Ni_x\ Fe_2O_4$ nanocomposites for hyperthermia applications

S.O. Aisida [a,b,c,d,e,*], T.C. Chibueze [a], M.H Alnasir [f], O.E. Oyewande [g], A.T. Raji [h,i], C.E. Ekuma [j], I. Ahmad [b,e], T-k. Zhao [e,k], M. Maaza [c,d], F.I. Ezema [a,c,d,l]

[a] *Department of Physics and Astronomy, University of Nigeria Nsukka, 410001, Nigeria*
[b] *National Centre for Physics, Quaid-i-Azam University Campus, Islamabad, 44000, Pakistan*
[c] *Nanosciences African Network, iThemba LABS-National Research, South Africa*
[d] *UNESCO-UNISA Africa Chair in Nanosciences/Nanotechnology, College of Graduate Studies, University of South Africa, MuckleneukRidge, P.O. Box 392, Pretoria, South Africa*
[e] *NPU-NCP Joint International Research Centre on Advanced Nanomaterials and Defects Engineering, NorthwesternPolytechnical University, 710072, China*
[f] *Department of Physics COMSATS University Islamabad, 44000, Pakistan*
[g] *Department of Physics, University of Ibadan, Ibadan, Nigeria*
[h] *School of Computing (SoC), College of Science, Engineering and Technology (CSET), University of South Africa (UNISA), Florida 1709, South Africa*
[i] *National Institute of Theoretical and Computational Sciences (NIThCS), South Africa*
[j] *Department of Physics, Lehigh University, Bethlehem, PA, 18015, USA*
[k] *School of Materials Science & Engineering, NorthwesternPolytechnical University, Xi'an, 710072, China*
[l] *Africa Centre of Excellence for Sustainable Power and Energy Development, University of Nigeria, Nsukka, Nigeria*

ARTICLE INFO

Keywords:
Cobalt nanoparticles
Hyperthermia
Microstructural
Surface absorption rate
Band-engineering

ABSTRACT

Magnetic hyperthermia-induced ferrite nanoparticles influenced by an external alternating magnetic field (AMF) are actively being pursued as a therapeutic tools for treating cancer tumor tissue. This work reports a combined experimental and computational study of pristine and Ni-doped cobalt ferrite. Specifically, cobalt ferrite ($CoFe_2O_4$) nanoparticles doped with nickel ions ($Co_{1-x}Ni_x\ Fe_2O_4$) with $0 \leq x \leq 0.6$ have been synthesized by *in-situ* sol-gel protocol to enhance the microstructural and magneto-optical properties. The formulated samples were evaluated using various characterization techniques. To further accentuate the properties of the synthesized samples, we used first-principles density functional theory (DFT) calculations to model the various cobalt ferrite compositions. The obtained results from DFT are in good pact with the structural, optical and the magnetic properties as observed in the experiment. Hence, our results demonstrate synthesis protocols and band-engineering routes to enhance the microstructural and magneto-optical properties of cobalt ferrite for magnetic hyperthermia applications.

1. Introduction

Magnetically induced hyperthermia (MIH), often called thermal ablation, involves the use of an alternating magnetic field (AMF) to give the magnetic nanoparticles (NPs) the requisite thermal energy to reorient the magnetic moment of the particle. MHI has been observed to be minimally living tissue invasive and tissue-specific. To improve the localization and target delivery to the tumor site, the NPs are heated using an external AMF. This thermal therapy of cancerous tumor cells operates by elevating the temperature of the tumor cells within the therapeutic temperature range, 40–46 °C [1,2].

Some parameters are expedient to determine the necessary temperature for cancerous tissue. These parameters strongly depend on the strength of the EMF, the selected magnetic materials, the frequency used, the time rate of application of the applied EMF, and the blood perfusion inside the cell [3]. For MIH to function optimally, the chosen parameters and the real-time temperature control are necessary to choose a magnetic material whose maximum temperature is equivalent to the therapeutic temperature.

For effective utilization, ferrite nanoparticles (FNPs) with tailored nano-framework and tunable physical, optical, chemical, mechanical and magnetic properties are at the forefront of providing non-invasive

---

* Corresponding author. Department of Physics and Astronomy, University of Nigeria Nsukka, 410001, Nigeria.
E-mail address: samson.aisida@unn.edu.ng (S.O. Aisida).

https://doi.org/10.1016/j.solidstatesciences.2022.107107
Received 23 September 2022; Received in revised form 26 December 2022; Accepted 30 December 2022

therapy for magnetic induced hyperthermia treatment for cancerous tissues [4–7]. FNPs are gaining more attention daily from different researchers than their bulk values. Spinel FNPs (SFNPs) possess unique properties that gave them special attention for sundry applications such as magnetic induced hyperthermia [8–15], magnetic resonance imaging (MRI) [9], drug delivery [16,17], antibacterial/photocatalytic activity [18–20], catalysis [21] and magnetic record/storage [22]. SFNPs are seriously under investigation, both for *in vivo* and *in vitro* potential candidates for therapeutic hyperthermia treatment of cancerous cells. This has helped localize the tumor's heating to make it less invasive and more cancerous cell-specific [23]. **S**FNPs have been auspicious in cancer treatment using magnetic hyperthermia [24]. Many have demonstrated the potency of this radio-frequency induced thermotherapy on dissimilar types of cancer like prostate, breast and brain cancers [25–28]. To minimize the toxicity effect, the number of nanoparticles used needs to be small while retaining the desired effect. For SFNPs to attain the therapeutic temperature with the minimal administered SFNPs on the specific tissue, the SFNPs are expected to exhibit high inductive SAR. The administered quantity of SFNPs depends on the saturation magnetization (M_s), magnetic anisotropy (K), the average particle size, the frequency and the magnetic field intensity [29].

Among these SFNPs, Cobalt ferrite nanoparticles (CFNPs) have received good attention by researchers owing to their unique features like inverse spinel structures, stable hexagonal close-packed at room temperature, stable face-centered cubic at 450 °C and above, high magneto-crystalline-anisotropy, narrow bandgap, chemical stability, good saturation magnetization (M_s), magnetic storage ability, high-frequency storage device, high anisotropy field, and high electrical, catalytic and magnetic performance. These make CFNPs a unique therapeutic tool in biomedical fields [30]. The method adopted for synthesizing FNPs is responsible for tailoring the cationic distribution, morphology, particle size, and the magnetic properties. Many synthesis protocols have been adopted to optimize the desired properties of the FNPs for diverse applications, chiefly, biomedical [31,32]. Common methods adopted by different researchers such as microemulsion [33], co-precipitation [34], sol-gel [35], thermal decomposition [36], biosynthesis [19], pulsed laser technique [37] and hydrothermal [38], are responsible for the different morphology and the variation in the particles size [39]. Besides the synthesis protocols, surface functionalization is another principal factor that defines the properties of FNPs chiefly for biomedical applications [40].

In this work, *in situ* sol-gel protocol has been adopted to synthesize and enhance the microstructural and magneto-optical properties of $CoFe_2O_4$. This is achieved by replacing Co cation with Ni at a varying concentration, i.e., $Co_{1\text{-}x}Ni_x\ Fe_2O_4$ x = $(0 \le x \le 0.6)$, suitable for hyperthermia applications. The samples' properties were analyzed with varieties of experimental techniques. To validate the experimental data and to gain a deeper understanding of the nature of electronic bonding and magnetization in the synthesized cobalt ferrite nanoparticles, we performed first-principles density-functional theory (DFT) calculations to model the properties of $Co_{1\text{-}x}Ni_x\ Fe_2O_4$ $(0 \le x \le 0.6)$ systems. The obtained properties are auspicious for magnetic hyperthermia applications. Following the introduction, in section 2, we presented the methods for the sample preparation, characterization techniques, and the first-principles approach. In Section 3, we presented the results and discussion and presented the conclusion in Section 4.

2. Materials sample preparation and characterization

2.1. Materials

Sigma Andrich product of ferric nitrate ($Fe(NO_3)_3{\cdot}9H_2O$), Cobalt nitrate ($Co(NO_3)_2{\cdot}6H_2O$) and Nickel nitrate ($Ni(NO_3)_2{\cdot}6H_2O$) in their analytical grade were procured commercially in Pakistan. These analytical grades were used as-received without further purification. Double-distilled water (DDW) was used all through the synthesis procedures.

2.2. In situ sol-gel synthesis of $Co_{1\text{-}x}Ni_x\ Fe_2O_4$ nanocomposites

Pure cobalt ferrite ($CoFe_2O_4$) and Ni-doped cobalt ferrite samples of different Ni concentrations ($Co_{1\text{-}x}Ni_x\ Fe_2O_4$, where x = 0, 0.3175, and 0.625 were prepared by a sol-gel method. The stoichiometric ratio of $Fe(NO_3)_3{\cdot}9H_2O$, $Co(NO_3)_2{\cdot}6H_2O$, and $Ni(NO_3)_2{\cdot}6H_2O$ oxidizing agents were homogenized in 100 mL of double-distilled water (DDW) and stirred at 800 rpm for 2 h. After 2 h, the sol mixture was thermally treated at 60 °C for 4 h while stirring to give a brownish gel-like solution. Ultrasonication of the obtained gel was done in a water bath at 30 °C for 1 h and the purified gel was transferred into the muffle furnace at 80 °C for 6 h. The $Co_{1\text{-}x}Ni_x\ Fe_2O_4$ nanoparticles formulated were calcined at 900 °C for 3 h in a biologic vacuum oven. To the solution of CFNPs, 50 mL solution of $Ni_x(x = 0.3175\ and\ 0.625)$ was introduced into the homogenized solution and stirred for an additional 2 h for the two concentrations, respectively. We have labeled the $CoFe_2O_4$, $Co_{1\text{-}x}Ni_x\ Fe_2O_4$ (x = 0.3175), and $Co_{1\text{-}x}Ni_x\ Fe_2O_4$ (x = 0.625) samples as C1, C2 and C3, respectively.

2.3. Characterizations techniques

The structural properties (average particle sizes) of the samples were examined using powder X-ray diffraction (XRD) spectroscopy (Shimadzu LabX 6100 diffractometer with Cu-kα radiation with a wavelength, $\lambda = 1.5418$ Å). UV–visible diffuse reflectance spectroscopy (UV-DRS Cary100) have been used to measure the absorption properties of the samples. The surface morphology was characterized by the Scanning electron microscopy (SEM) (JEOL 6400), while transmission electron microscopy (TEM) and selected area electron diffraction (SAED) patterns were obtained using a Tecnai G^2 F20 S-Twin High-Resolution TEM (HRTEM) operated at 200 kV. Also, thermogravimetric analysis (TGA) (DTG-60H Shimadzu) was performed in the temperature range of 49–995 °C in an inert gas environment to determine the material mass as a function of temperature and time. Fourier Transform Infrared (FT-IR) Spectrometer (PerkinElmer FT-IR spectra 1650, USA) was used to detect the functional groups in the samples while Raman spectroscopy (DV420_OE Model Japan, 1470 HZ) was used to obtain the structural and chemical information about the samples. Finally, the magnetization of the samples was determined using vibrating sample magnetometer (VSM) (Quantum Design Versa lab Measurement).

2.4. Computational method

The primitive unit cell of spinel $CoFe_2O_4$ consists of 14 atoms with an experimental lattice parameter of $a_{expt} = 8.385$ Å (Fig. 1a). It has two types of lattice sites for the cation occupancy, namely the tetrahedral and octahedral, often referred to as the A and B sites, respectively. Co^{2+} occupies the tetrahedral A sites in a normal spinel structure while Fe^{3+} sits on the octahedral B sites. However, in an inverse spinel structure, Fe^{3+} ions occupy the A site while the B sites are populated by both the Co^{2+} and Fe^{3+} ions (Fig. 1b). To model the pristine $CoFe_2O_4$ and Ni-doped $CoFe_2O_4$, i.e., $Co_{1\text{-}x}Ni_x\ Fe_2O_4$ (x = 0.31 and 0.62), we have used the supercell method wherein we expand the lattice parameter of the primitive unit cell according to a_{calc} (2 × 2 × 2), where a_{calc} is the computed lattice parameter (Fig. 1b). This cobalt ferrite supercell of 112 atoms consists of 16 Co, 32 Fe, and 64 O atoms, which is large enough to avoid dopant-dopant interactions and for the required doping concentration in the modeled structures. The Ni-doped atomic structures were produced using the quasi-random site occupancy disorder approach [41] with the mcsqs utility within the Alloy Theoretic Automated Toolkit [42] package. Specifically, $Co_{1\text{-}x}Ni_x\ Fe_2O_4$ (x = 0.3175) are produced by the random substitution of five Co atoms with Ni atoms in the supercell $Co_{1\text{-}x}Ni_x\ Fe_2O_4$ (x = 0.625), ten of the Co atoms in the supercell are substituted with the Ni atoms. These modeled structures

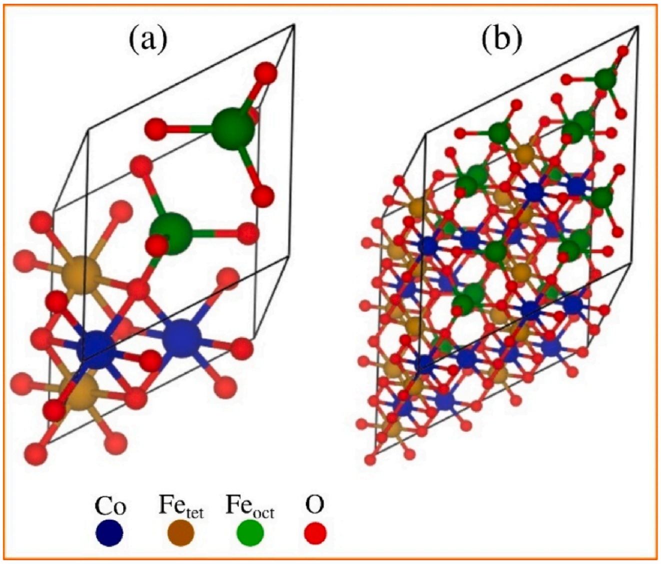

Fig. 1. (a) Primitive unit cell of cobalt ferrite, $CoFe_2O_4$ (b) Supercell of size 2 × 2 × 2 used for the defect calculations. Blue, gold, green and red atoms denote cobalt, iron (Tetrahedral), iron (octahedral) and oxygen atoms respectively. (For interpretation of the references to colour in this figure legend, the reader is referred to the Web version of this article.)

closely mimic $Co_{1\text{-}x}Ni_x\ Fe_2O_4$ (x = 0.3175) and $Co_{1\text{-}x}Ni_x\ Fe_2O_4$ (x = 0.625) as in the experimental samples.

After obtaining the relaxed structures, spin-polarized density functional theory calculations [43,44] based on generalized gradient approximation (GGA) functional of the Perdew-Burke-Ernzerhof (PBE) type [45] are performed on the pristine and Ni-doped $CoFe_2O_4$, using the Quantum-Espresso (QE) code [46]. Ion and valence electron interactions have been represented with scalar relativistic norm-conserving pseudo potentials [47] obtained from the Pseudo Dojo library [48,49] with Fe 3s, 4s, 3p, 3d; Co 3s, 4s, 3p, 3d; Ni 3s, 4s, 3p, 3d; O 2s, 2p as the valence orbitals. To sample the first Brillouin zone, we employed a 2 × 2 × 2 k-point with the Monkhorst-Pack scheme [50]. We used 80 Ry (320 Ry) for the kinetic energy (charge density) cut-offs and all the calculations are converged to 1 mRy/atom and 1 mRy/au, respectively, for the energy and Hellmann-Feynman force. To account for the itinerate electrons on Fe, Ni, and Co, we added an onsite Coulomb repulsion term U_{eff} to the PBE functional using the rotationally invariant procedure proposed by Dudarev et al., [51]. We have applied U_{eff} of 5 eV [52], 5.9 eV [53], and 4.8 eV [54] from the literature on the d-orbitals of Fe, Co, and Ni, respectively.

3. Results and discussions

3.1. Structural study of the samples

The structural analyses presented in Fig. 2a showed the XRD study of $Co_{1\text{-}x}Ni_x\ Fe_2O_4$ ($x = 0 \leq x \leq 0.6$). The diffraction peaks showed that the formulated samples were crystalline with the 2θ values and crystallographic planes of 30.2° (220), 35.5° (331), 43.2° (400), 53.6° (422), 57.2° (511), 62.8° (440) and 74.2° (533). This confirmed the cubic spinel structure phase of the formulated samples. The broad peaks obtained show that the particles are in nanosize range with diffraction peaks well matched with the JCPD card NO- 22-1086 [55]. The average crystallite size ($\varphi_{Avr.}$) obtained by Debye-Scherer's equation Eq. (1), presented in Table 1, is between 18 and 22 nm.

$$\varphi_{Avr.} = \frac{0.9\,\lambda}{\beta\ Cos\ \theta} \tag{1}$$

$$d = \frac{\lambda}{2\ sin\ \theta} \tag{2}$$

Table 1
The average crystallite size ($\varphi_{Avr.}$), the lattice parameter (d), bandgap (E_g), and the micro-strain (ψ) of $Co_{1\text{-}x}Ni_x\ Fe_2O_4$as obtained from the X-ray diffraction of various undoped and Ni-doped $CoFe_2O_4$ samples.

Sample	Plane	β (nm)	2 θ (°)	$\varphi_{Avr.}$ (nm)	d (nm)	E_g (eV)	ψ
$CoFe_2O_4$	311	0.46128	35.47	18.8	0.1327	1.52	0.0939
$Co_{1\text{-}x}Ni_x$ **Fe_2O_4 (x = 0.3175)**	311	0.41734	35.55	20.8	0.1325	1.54	0.0849
$Co_{1\text{-}x}Ni_x$ **Fe_2O_4 (x = 0.625)**	311	0.39452	35.52	22.0	0.1326	1.55	0.0803

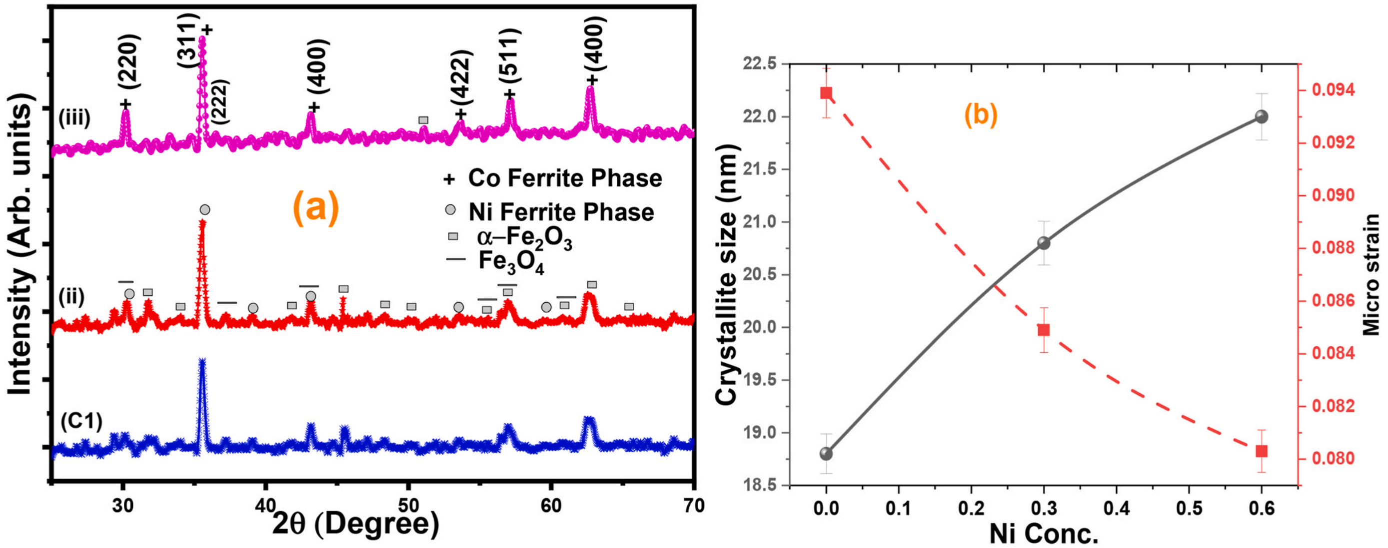

Fig. 2. (a) XRD analysis of (i) $CoFe_2O_4$, (ii) $Co_{1\text{-}x}Ni_x\ Fe_2O_4$ (x = 0.3175) and (iii) $Co_{1\text{-}x}Ni_x\ Fe_2O_4$ (x = 0.625) (b) comparison between crystallite size and the microstrain with respect to Ni ions.

$$\psi = \frac{\beta \, Cos \, \theta}{4} \tag{3}$$

where φ is the average crystallite size (nm), λ is the X-rays wavelength ($\lambda = 0.15406$ nm), β is the full width at half maximum (FWHM) intensity measured in radians and θ is the Bragg diffraction angle of the plane [56]. Also, the lattice spacing (*d*) was evaluated using the Bragg equation (Eq. (2)). The micro-strain (ψ) of the samples from the (311) plane due to the localized disturbance of the lattice was estimated using (Eq. (3)) [57]. The ψ was observed to decrease as the crystallite size increases, as shown in Fig. 3 (b). Hence, the effect of Ni concentration on the micro-strain and the crystallite size in the formulation of $Co_{1\text{-}x}Ni_x$ Fe_2O_4 is presented in Table 1 and Fig. 2 (b).

3.2. Morphological study of the samples

The morphological study of the samples determined by SEM has been presented in Fig. 3(a–c). The SEM images showed that sample C1 as shown in the inset of Fig. 3 (a), gives a cubic-like shape with inhomogeneous agglomerated particles. The cubic nature of the particles with a better homogeneity which decreases in particle size was observed in sample C2 as presented in the inset of Fig. 3 (b). Spherical nanograins were seen as the concentration of Ni ion increases, as observed in sample C3 presented in the inset of Fig. 3 (c). As shown in Fig. 3(d–f), the particle size distribution obtained using ImageJ software decreases considerably as Ni ions concentration increases. The particle size reduction is due to the introduction of Ni ions in the solution to attain a suitable size for biomedical applications. The decrease in the particle size, we presume is due to the ionic distribution of Ni ion and perhaps the different growth rates of the crystals in the samples. Similar results of the cubic shape of $Co_{1\text{-}x}Ni_x$ Fe_2O_4 with aloe vera were obtained by Unchista et al. [58]. The inhomogeneity in the samples was also observed by Kavas et al. in $NiFe_2O_4$ doped with Zn synthesized by PEG-assisted hydrothermal method [59]. The EDS analysis, presented in Fig. 3 (g, h and i), established the essential elements having Fe with the strongest peak at 6.4 keV, and other elements with strong peaks are Co, Ni, and O; these constituent elements confirmed the formulation of $Co_{1\text{-}x}Ni_x$ Fe_2O_4. The cubic nature of $Co_{1\text{-}x}Ni_x$ Fe_2O_4 formulated was further examined with TEM, as presented in Fig. 3 (j - l). The TEM micrograph further accentuated the cubic nature of the samples.

3.3. Optical properties study of the samples

The optical properties were analyzed using DRS. The energy bandgaps as presented in Fig. 4 were evaluated using the formula of Kubelka-Munk (KM) and Tauc plot using reflectance data as presented in Eqs. (4)–(9).

$$F(R) = \frac{\mu}{s} = \frac{(1-R)^2}{2R} \tag{4}$$

where F(R) is the Kubelka-Munk function with

$$\mu = (1-R)^2 \tag{5}$$

$$s = 2R \tag{6}$$

$$R = \frac{\%R}{100} \tag{7}$$

The samples' bandgap energies through the Tauc plot's extrapolation to $[F(R).h\upsilon]^{n/2} \approx 0$ were valued from the direct allowed transition.

$$(F(R).h\upsilon)^{n/2} \; vs \; .h\upsilon \text{ for } (n = 4) \tag{8}$$

$$(\mu h\nu)^2 = A\left(h\nu - E_g\right) \tag{9}$$

The energy bandgaps of the samples as presented in Table 1 were obtained with a plot of $(\mu h\nu)^2$ against $h\nu$ from Eq. (9) [60,61]. The obtained energy bandgap increases slightly from 1.52 eV for the pristine $CoFe_2O_4$ to 1.54 eV and 1.55 eV for the $Co_{1\text{-}x}Ni_x$ Fe_2O_4 (0.3175) and $Co_{1\text{-}x}Ni_x$ Fe_2O_4 ($x = 0.625$), respectively, i.e., as the Ni ions concentration increases. Studies have shown that the energy bandgap of nanomaterials is often swayed by the structural or crystal parameters [62]. These observations are also consistent with the previous report by Sagar et al. [61]. The information obtained from the energy bandgap of the nanoparticles is beneficial to obtain a better understanding of the quantum size effect through the absorption edge.

3.4. Raman study of the samples

Raman spectroscopy analysis is a special technique used to explore nanoparticles' atomic structure [63]. The Raman spectra prediction by the optical phonon distribution is given by 5T1u + A1g + Eg + 3T2g. The 5T1u and (A1g + Eg + 3T2g) modes are active in the infrared (IR) and Raman respectively, which composed A-site, B-site and O ions in the $Fe_2Co_{1\text{-}x}Ni_xO_4$ spinel structures [64]. The A1g (symmetric stretching) and Eg (symmetric bending of the oxygen anion) modes, while the T2g mode is owing to the asymmetric stretching of the oxygen anion in line with the tetrahedral and octahedral cations [65]. The Raman spectroscopy spectra analysis as shown in Fig. 5 and presented in Table 2 of the as-prepared sample with the Raman mode ≈673 cm^{-1} and the subsidiary at the lower wavenumber ≈617 cm^{-1} are designated to the A1g (1) and A1g (2) modes respectively, showing the stretching vibration of Fe–O and X–O (divalent metals) in the tetrahedral sites. The other lower Raman modes at 572, 437, 262, and 201 cm^{-1} wavenumbers were apportioned to the T2g (1), T2g (2), Eg, and T2g (3), signifying the pulsation of the spinel structure. A slight Raman modes shift was also observed in all the samples as the concentration of Ni ion increased [64]. This may be due to the cation re-distribution in the $Co_{1\text{-}x}Ni_x$ Fe_2O_4 as the concentration of Ni ions varies. This observation also agrees with the study by Raghvendra et al. which considered honey mediated $CoFe_2O_4$ nanoparticles by sol-gel method [66].

3.5. Magnetic properties study of the samples

The hysteresis loop of magnetization (M) against the magnetic field (H) conducted at room temperature (T_R) as presented in Fig. 6 (a) revealed the different magnetic properties of $Co_{1\text{-}x}Ni_x$ Fe_2O_4 influenced by Ni ions concentration. The magnification of the inset as presented in Fig. 6 (b), gives better information about the magnetic properties of the samples. Ferrimagnetic nature was observed for all the samples, i.e., the magnetization loop that did not pass through the origin, and this formation retains remanet magnetization (M_r) at zero magnetic fields. The saturation magnetization (M_s) decreases as the Ni ions concentration increases, as presented in Table 3. The perceived decrease in M_s is owing to the cation site distribution in the spinel ferrite structure; this agrees with the results reported by Unchista et al. [58]. The H_c measures the magnetic field in the inverse direction apportioned to force M_r back to zero. The H_c was also observed to decrease as the Ni ions concentration increased. The increase in Ni ions concentration changed the magnetic properties from strong ferromagnetism to ferrimagnetic (i.e, towards superparamagnetism), as shown in Fig. 6 (b). Similar results were also observed in the study by Chithra et al. on Zn substituted cobalt ferrite [67].

The samples' anisotropy constant and magnetic moment in Bohr magneton (n_B) were determined using Eqs. (10) and (11), respectively [68]. These values were observed to decrease as the Ni ion concentration increases, as presented in Table 3.

$$K = \frac{M_s \times H_c}{0.96} \tag{10}$$

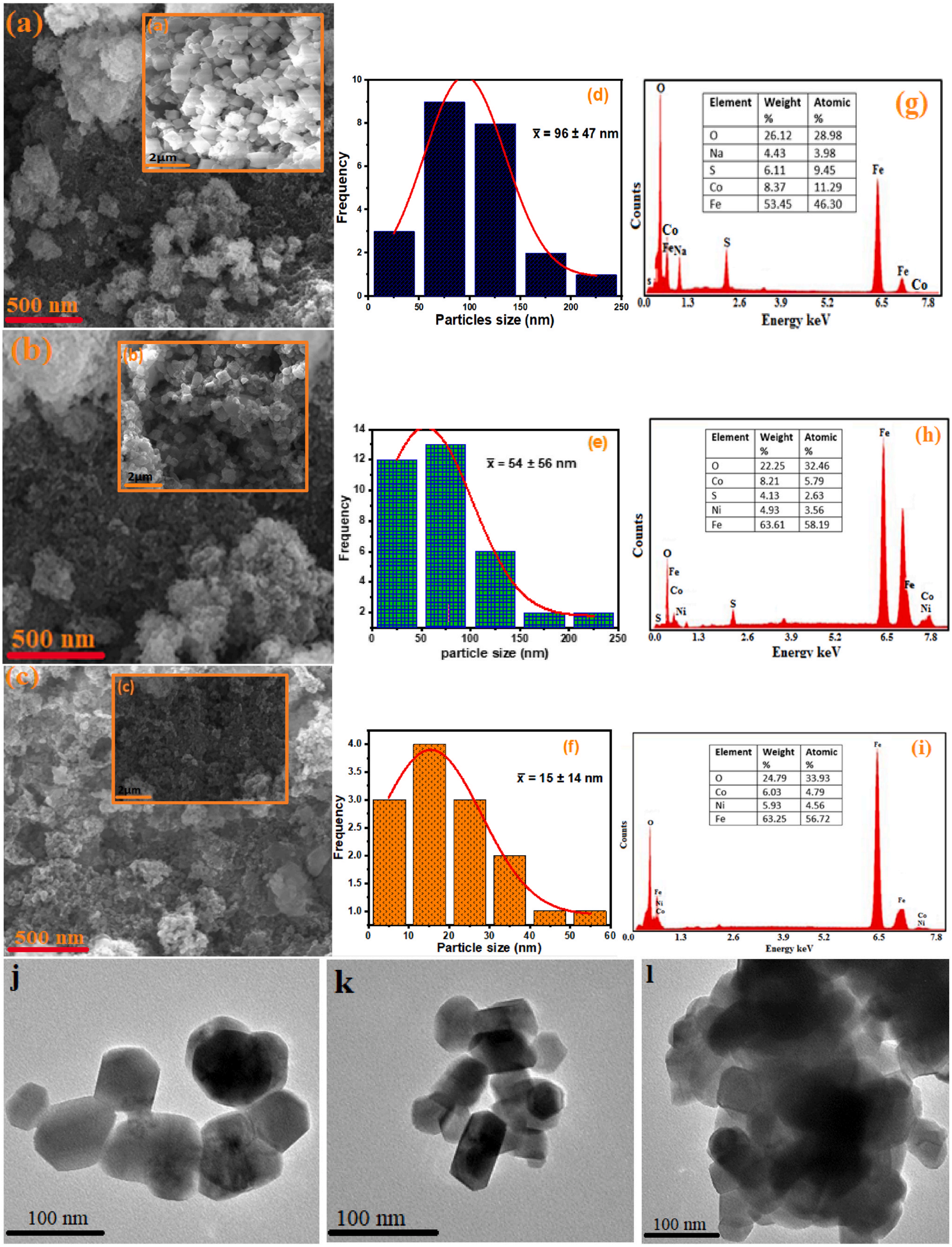

Element	Weight %	Atomic %
O	26.12	28.98
Na	4.43	3.98
S	6.11	9.45
Co	8.37	11.29
Fe	53.45	46.30

Element	Weight %	Atomic %
O	22.25	32.46
Co	8.21	5.79
S	4.13	2.63
Ni	4.93	3.56
Fe	63.61	58.19

Element	Weight %	Atomic %
O	24.79	33.93
Co	6.03	4.79
Ni	5.93	4.56
Fe	63.25	56.72

Fig. 3. (a–c) SEM micrograph (d–f) particle size distribution (g–i) EDS analysis, (j–l) TEM images of (i) $CoFe_2O_4$, (ii) $Co_{1-x}Ni_x Fe_2O_4$ ($x = 0.3175$) and (iii) $Co_{1-x}Ni_x Fe_2O_4$ ($x = 0.625$), respectively.

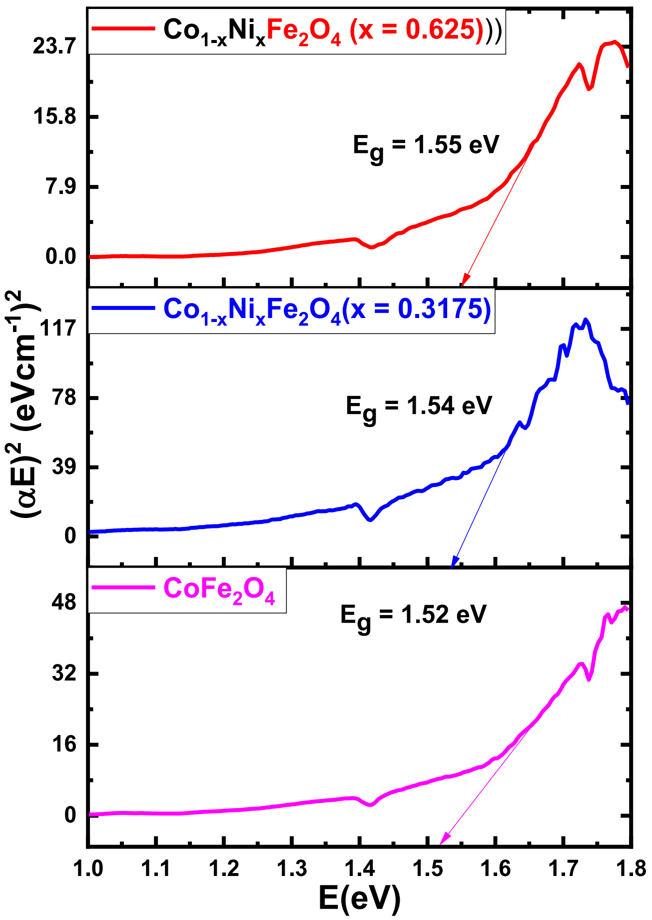

Fig. 4. The energy bandgap of the samples.

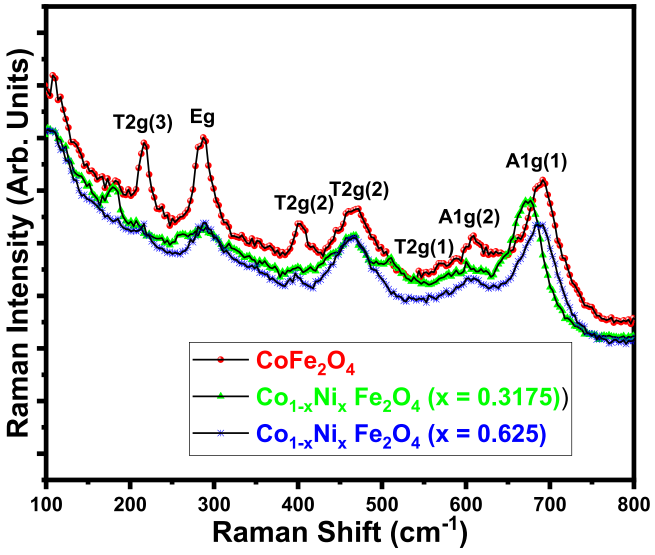

Fig. 5. Raman spectra of $Co_{1-x}Ni_x$ Fe_2O_4.

$$n_{B/fu} = \frac{M_W \times M_s \times 10^{-3}}{N_A \times \mu_B} \tag{11}$$

where $n_{B/fu}$, M_W, N_A, μ_B, K and are the magnetic moment per formula unit (in Bohr magneton,μ_B), the molecular weight of the precursor (mg/mole), Avogadro's number ($N_A = 6.02 \times 10^{23} mol^{-1}$), the magnetic moment of electron ($\mu_B = 9.27 \times 10^{-24} Am^2$) and anisotropy constant (erg/g), respectively.

Table 2
Raman modes of $Co_{1-x}Ni_x$ Fe_2O_4.

Raman peaks (cm^{-1})						
Samples	T2g (3)	E_g	T2g (2)	T2g (1)	**A1g** (2)	A1g (1)
$CoFe_2O_4$	215	286	468	568	606	691
$Co_{1-x}Ni_xFe_2O_4$ **(x = 0.3175)**	208	286	468	563	603	673
$Co_{1-x}Ni_xFe_2O_4$ (x = 0.625)	215	286	468	574	605	688

The decrease in M_s, K and n_B we believed is due to the concentration of Ni ions in the formulated samples. As a result, the A-B (A-tetrahedral site, B-octahedral site) exchange interaction is well established, with ≈20% Co residues assigned to the A-site [69]. Hence, according to the Néel model, the cation inversion distribution seen in A-B interstitial sites is often better than the interactions in A-A, and B–B interactions [70–72]. The characteristic and reorientation of the magnetic materials directions is determined by the remanence ratio of M_r/M_s to the nearby axis after removing the magnetic field [73]. The M_r/M_s of our samples is between ≈0.16 and ≈0.49; these values signify uniaxial anisotropy-dominated behavior of our samples in comparison to ≈0.83 (the maximum expected value for cobalt ferrite) [74]. The grain size also shows a significant role in the decrease of the M_s with the concentration of Ni. This was observed to be smaller than the bulk value of 93.9 emu/g as a result of the cation distribution and surface defect [71,75,76]. The M_r and the H_c decrease towards forming a single domain, which may attain the superparamagnetic nature as the concentration of Ni ions increase further, as observed in sample C_3. The M_s, H_c, M_r, η_B, M_r/M_s and K are all Ni ions concentration-dependent, as shown in Fig. 6 (c & d).

3.6. *Magnetic hyperthermia analysis of the samples*

The heating analysis was conducted using Magnetherm Nanotherics (MN) (COMDEL CLF-5000, USA RF generator) operating at a frequency of 425 kHz with AMF at 145 Oe for all the samples dispersed in Double Distilled Water (DDW). 20 mg each of $Co_{1-x}Ni_x$ Fe_2O_4 (x = 0, 0.3175, 0.625) samples were dispersed in 1 mL of DDW and were allowed to sonicate for 10 min. The self-heating plots of time rate in temperature of the samples were then obtained; the specific absorbance rate (SAR) from the characteristics of the synthesized samples were evaluated using the formula described in Eq. (12).

$$\text{SAR } (Co_{1-x}Ni_x\ Fe_2O_4) = C \bullet \frac{\Delta T}{\Delta t} \bullet \frac{M_s}{M_w} \tag{12}$$

where, C = 4.180 J/g/^{o}C) ; M_s is the mass of the sample; M_w the molar mass of the sample and $\frac{\Delta T}{\Delta t}$ is the heating gradient.

The hyperthermia by self-heating analysis as presented in Fig. 7 (a) yields a momentous temperature change of the samples under AMF of 145 Oe. The first stage witnessed a sharp rise in the temperature, which continued gradually after a while, as presented in Fig. 7 (a). The maximum temperature was observed to reduce as the concentration of Ni ions increases until the therapeutic temperature range (40–48 °C) is attained [8,77,78]. The different fields also play a vital role in the heating temperature, as observed in Fig. 7 (b). Sample C_3 was further subjected to 165 Oe and 185 Oe AMF, as presented in Fig. 7 (b). An increase in the maximum temperature as the magnetic field increased was observed. Earlier studies showed that hyperthermia's rapid increase in temperature is also frequency-dependent. As the frequency increases, the temperature rise also increases [79,80]. The sharp self-heating curve initiated in the first phase is due to the associated magnetic field and the magnetic losses, which gradually lead to the second phase with a gradual increase; this is allied to the hysteresis loss [81–83]. The

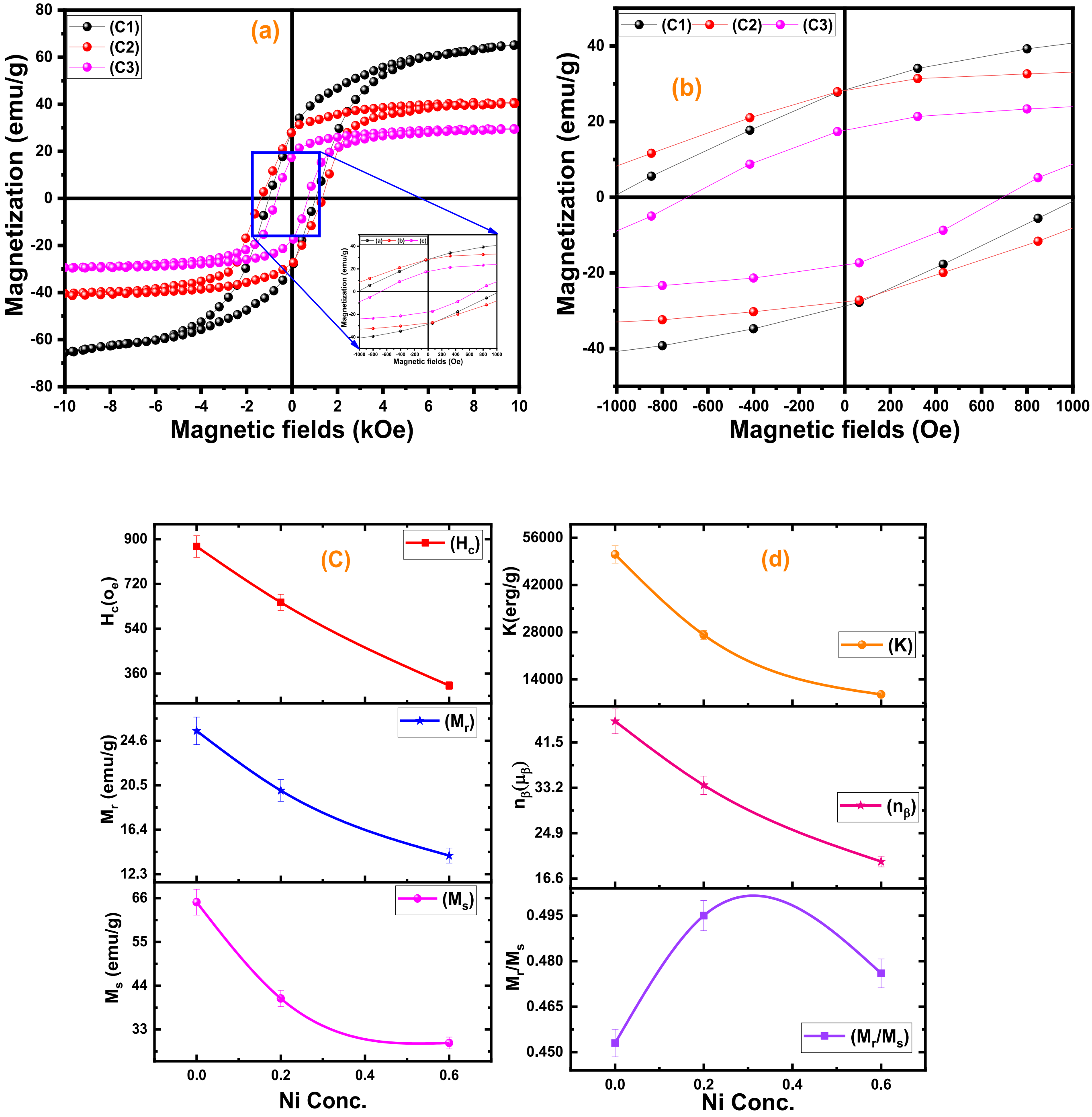

Fig. 6. (a) Hysteresis loop (b) magnification of the inset (c) M_r, M_s, and H_c against Ni (d) M_r/M_s, η_B and K against Ni concentration of the compound.

Table 3
Magnetic parameters of the samples.

Samples	M_s (emu/g)	M_r (emu/g)	H_c (O_e)	M_r/ M_s	η_B (μ_B)	K (erg/ g)
$CoFe_2O_4$	65.00	25.51	870.36	0.39	(2.69)	51,070
$Co_{1-x}Ni_xFe_2O_4$ **(x = 0.3175)**	40.79	20.00	645.90	0.49	(1.71)	27,195
$Co_{1-x}Ni_xFe_2O_4$ **(x = 0.625)**	29.61	14.02	311.50	0.47	(1.24)	9552

obtained result is highly auspicious compared to other previously obtained results [81,84]. Heat loss procedures in blocked single-domain/multi-domain are due to hysteresis loss, while in un-blocked single-domain, the heat loss is principally owing to the Néel or Brownian losses [85,86].

The specific absorption rate (SAR) using 145 Oe applied field was evaluated using Eq. (12). The obtained SAR increases for the M_s and decreases with respect to Ni ions as shown in Table 4 and Fig. 7 (c & d). The time rate of change of temperature value with the SAR also decreases and is within 40–48 °C. Sample $Co_{1-x}Ni_xFe_2O_4$ (x = 0.625) has proven to be more enhanced and most suitable for Hyperthermia applications to salvage the side effect challenges with moderate SAR value

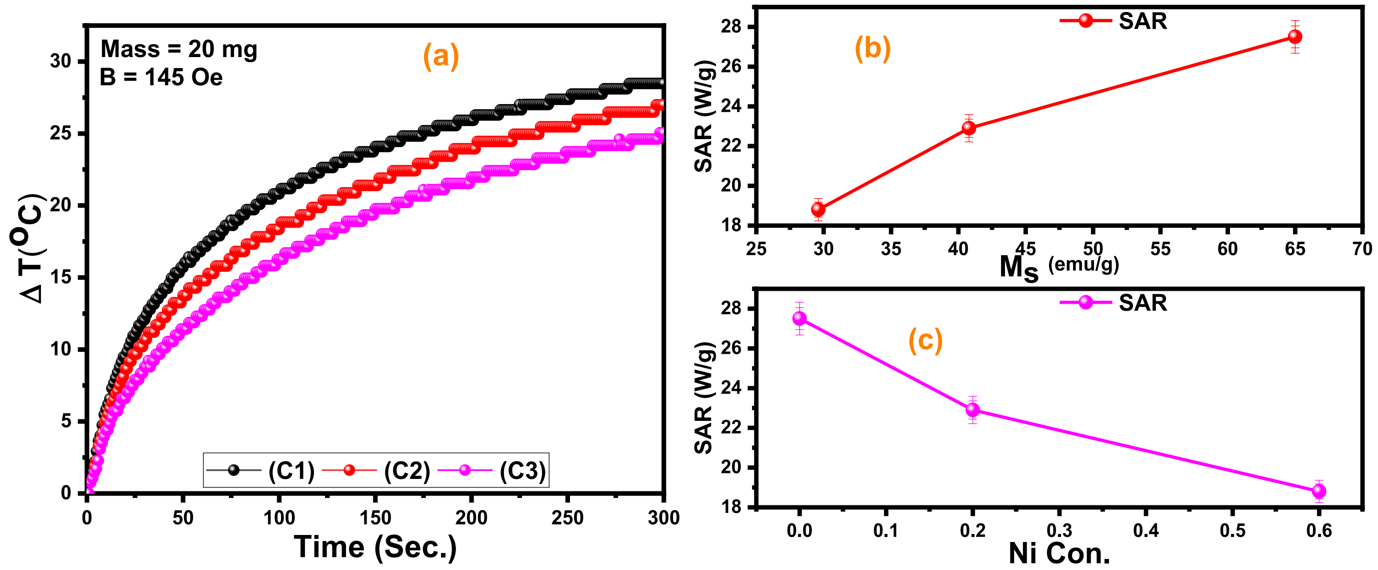

Fig. 7. (a) Heating abilities of $Co_{1-x}Ni_xFe_2O_4$ at 145 Oe (b & c) SAR measurement against M_s and concentrations of Ni ions respectively.

Table 4
SAR parameters with the magnetic field of 145 Oe and frequency of 425 kHz.

Compounds	Conc. (mg/mL)	B (Oe)	Slope (°C/sec)	SAR (W/g)	Max. Temp. (°C)
$CoFe_2O_4$	20	145	0.33	27.50	49.70
$Co_{1-x}Ni_xFe_2O_4$ **(x = 0.3175)**	20	145	0.27	22.90	47.40
$Co_{1-x}Ni_xFe_2O_4$ **(x = 0.625)**	20	145	0.22	18.80	45.20

within the therapeutic range. This value is suitable for moderate hyperthermia applications. The obtained SAR value agrees with the works of kombaiah et al. [87], and is higher than several other systems [88, 89]. Other similar results are 319 W/g by Matsuda et al. for $CoFe_2O_4$ [90]. 19 W/g by El-Sayed et al. for $MgFe_2O_4$ [91] and 68.7 W/g by Doaga et al. for $MnFe_2O_4$ [92]. We note that our samples show a higher magnetothermal response at such a lower field and frequency as compared to previously reported results. Studies have shown that SAR value mostly depends on the structural and magnetic parameters (like saturation magnetization, effective anisotropy constant and particle size) and experimental parameters (such as radiofrequency amplitude and frequency), which could combine to produce high SAR in these samples [93,94] as observed in our samples. It has been observed that, maximum heating temperature of our samples lie within therapuatic range. Barati et al. reported the maximum heating temperature of samples lies within 315–319 K having maximum temperature close to the therapuatic range i. e $T_C = 319$ K [95], because sample generate heating in a ferromagnetic state and become paramagnetic above the therapuatic range i.e. it imposes an intrinsic check on the heat dissipation of the magnetic nanoparticles, thereby avoiding the possibility of spot-burning and overheating in magnetothermal therapy. At present we are investigating methods of producing polymer imbedded magnetic nanoparticles to improve their biocompatibility for studies of cytotoxicity of these materials.

3.7. DFT results of the samples

3.7.1. Structural properties

The DFT calculated ground state of inverse spinel $CoFe_2O_4$ has a lattice constant of $a_{calc} = 8.362$ Å. For the Ni-doped structures $Fe_2Co_{1-x}Ni_xO_4$ (x = 0.3125) and $Co_{1-x}Ni_xFe_2O_4$ (x = 0.625) and 0.625), we obtained a_{calc} of 8.334 Å and 8.328 Å, respectively. This shows a slight decrease in the lattice parameter of pristine $CoFe_2O_4$ due to the incorporation of Ni ions in qualitative harmony with the experimental observation (Table 1). The configurations of the doped structures are shown in Fig. 8 (a) and (b). Recal that in the inverse spinel structure, all the Co atoms and some Fe atoms occupy the tetrahedral site while the rest occupy the octahedral site. Thus, the slight decrease observed in the lattice constant of the doped systems as the dopant concentration increases could be ascribed to the reason that the ionic radius of Ni atom ~1.24 Å is slightly smaller than that of Co atom ~1.25 Å [96].

3.7.2. Electronic properties

To accentuate the electronic properties of the pristine and doped compounds, we present in Figs. 9–11 the band structure of the electronic calculated and the associated density of states obtained within the DFT

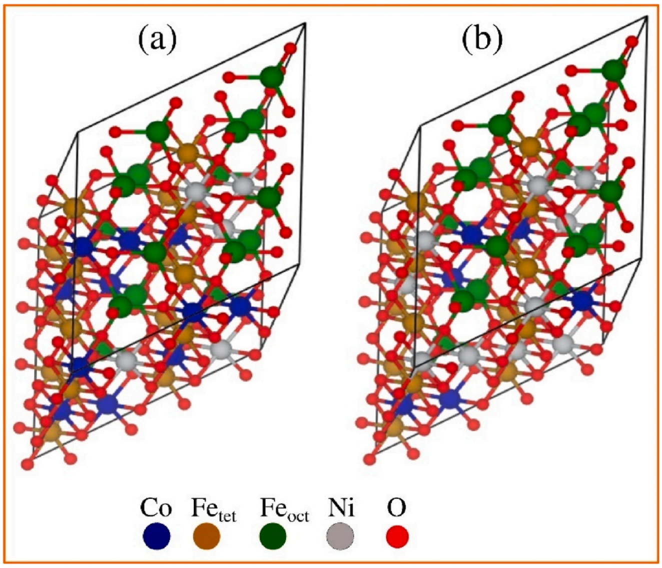

Fig. 8. (a) Conventional unit cell of Fe_2CoO_4 in the cubic spinel phase. (b) A 2 × 2 × 2 primitive unit cell used to model the defect structure. Blue, gold, ash and red atoms denote the cobalt, iron, nickel and oxygen atoms, respectively. (For interpretation of the references to colour in this figure legend, the reader is referred to the Web version of this article.)

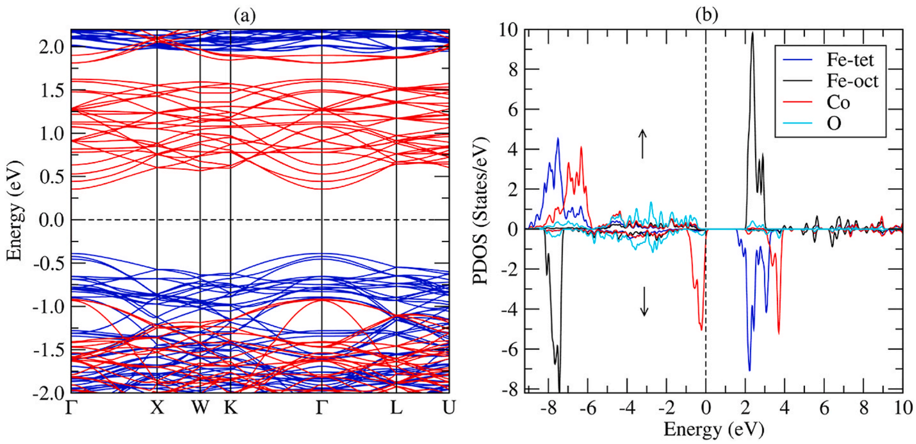

Fig. 9. (a) Band structure of pristine inverse spinel Fe_2CoO_4. The blue lines represent the spin-up bands, while the red line represents the spin-down bands. The horizontal dashed line at zero of energy is the Fermi level. (b) Atom and spin projected density of states (PDOS) for the pristine inverse spinel Fe_2CoO_4. The Fermi level is the vertical dotted line at zero on the energy axis. Positive values (upper panel) of the PDOS represent the majority-spin states, while the negative values (lower panel) represent the minority-spin states. (For interpretation of the references to colour in this figure legend, the reader is referred to the Web version of this article.)

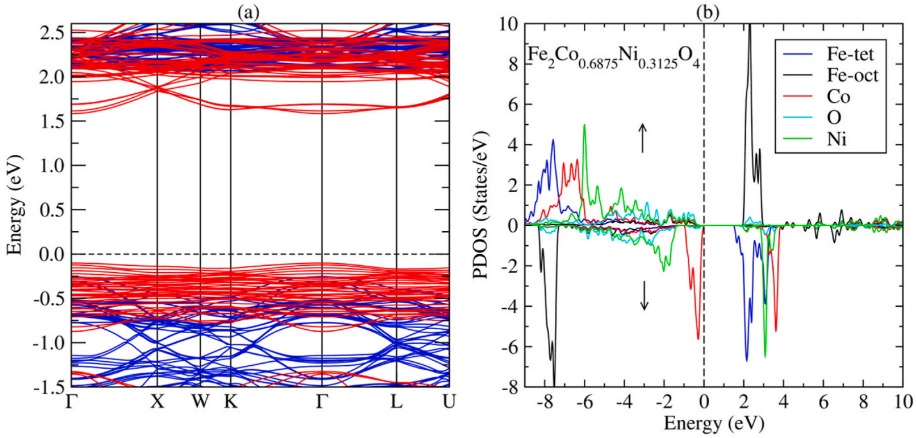

Fig. 10. (a) Band structure of pristine inverse spinel $Co_{1-x}Ni_xFe_2O_4$ (x = 0.3125). The blue lines represent the spin-up bands, while the red line represents the spin-down bands. The horizontal dashed line at zero of energy is the Fermi level. (b) Atom and spin projected density of states (PDOS) of the pristine inverse spinel $Co_{1-x}Ni_xFe_2O_4$ (x = 0.3125). The Fermi level is the vertical dotted line at zero on the energy axis. Positive values (upper panel) of the PDOS represent the majority-spin states, while the negative values (lower panel) represent the minority-spin states. (For interpretation of the references to colour in this figure legend, the reader is referred to the Web version of this article.)

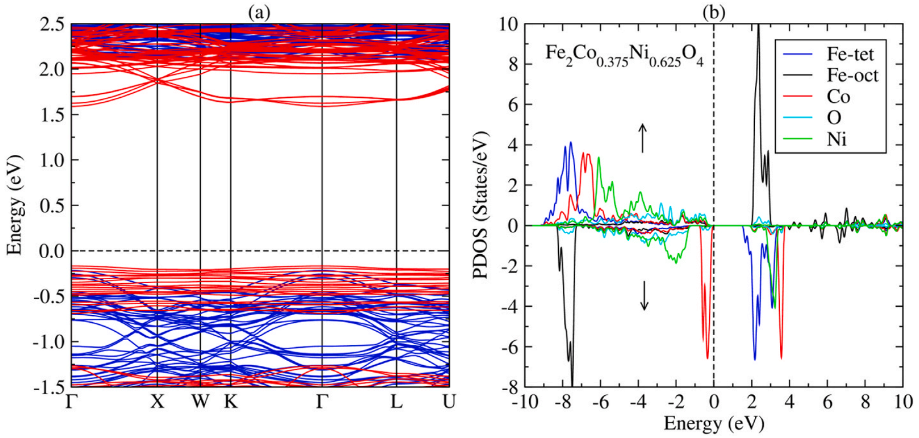

Fig. 11. (a) Band structure of pristine inverse spinel $Co_{1-x}Ni_xFe_2O_4$ (x = 0.625). The blue lines represent the spin-up bands, while the red line represents the spin-down bands. The horizontal dashed line at zero of energy is the Fermi level. (b) Atom and spin projected density of states (PDOS) of the pristine inverse spinel $Co_{1-x}Ni_xFe_2O_4$ (x = 0.625). The Fermi level is the vertical dotted line at zero on the energy axis. Positive values (upper panel) of the PDOS represent the majority-spin states, while the negative values (lower panel) represent the minority-spin states. (For interpretation of the references to colour in this figure legend, the reader is referred to the Web version of this article.)

+ *U* formalism. Our results show that the pristine and $Co_{1-x}Ni_xFe_2O_4$ (x = 0.3125, 0.625) are direct bandgap semiconductors with a bandgap of ~1.5 eV at the Γ-point. This calculated electronic bandgap is consistent with the experimental band gap of 1.52 and 1.55 eV as recorded for the pristine and doped $CoFe_2O_4$ (Table 1 and Fig. 4). The atomic projected density of states presented in Figs. 8 (b), 9 (b), and 10 (b) show that the top of the valence band is made of mainly of Co 3*d* minority spin states while the bottom of the conduction band is composed of Fe 3*d* minority spin states. The presence of the Ni dopant atoms states are not very significant around the Fermi level as such, has minimal effect on the size and nature of the electronic energy bandgap and the consequent low-energy physics.

3.7.3. *DFT magnetic properties of the samples*

The ferrimagnetic ground state was obtained for the inverse spinel $Co_{1-x}Ni_xFe_2O_4$. The total magnetic moment per formula unit and the local magnetic moment of the constituent atoms were calculated within the framework of DFT + *U* and presented in Table 5. Interestingly, the total magnetic moment per formula unit (fu) decreases as the concentration of Ni dopant increases. This is consistent with the experimental

Table 5
Magnetic properties of the inverse spinel $Co_{1-x}Ni_xFe_2O_4$. The local magnetic moment (in Bohr magneton, μ_B) on the Co atom (η_{Co}), local magnetic moment on Fe atom (η_{Fe}), local magnetic moment on Ni atom (η_{Ni}), local magnetic moment on O atom (η_O), and total magnetic moment per formula unit (η_B/f.u) of the compound.

Compounds	η_{Co} (μ_B)	$\eta_{Fe\text{-}tet}$ (μ_B)	$\eta_{Fe\text{-}oct}$ (μ_B)	η_{Ni} (μ_B)	η_O (μ_B)	η_B/f.u (μ_B)
$CoFe_2O_4$	2.8308	4.0320	- 4.0985	–	−0.0619	2.5168
$Co_{1-x}Ni_xFe_2O_4$ (x = 0.3175)	2.8014	3.9984	−4.1086	1.7607	−0.0777	2.0554
$Co_{1-x}Ni_xFe_2O_4$ (x = 0.625)	2.8082	4.0054	−4.1042	1.7274	−0.0871	1.6854

observation as reported in Table 4 (i.e., η_B column). Indeed, apart from reproducing the trend of decreasing magnetic moment with increasing concentration of Ni dopant, the DFT calculations produce magnetic moments (η_B/f.u column, Table 5) which are in reasonable harmony with the experimental value. The small discrepancies between the calculated and the experimental η_B may be due to the differences between the actual experimental condition of the samples and DFT model systems since the latter is only an idealization of the former. Also, the reason for the decrease in η_B with Ni inclusion may be related to the smaller local magnetic momrnt.

the moment of the Ni atoms compared to the Co atoms. It should be recalled that theoretically, a free Ni^{2+} (3 $d^{8)}$) ion has a magnetic moment of 1 μ_B while Co^{2+} (3 d^7) has a magnetic moment of 3 μ_B. Thus, it is plausible to expect that replacing Co with Ni as done in $Fe_2Co_{1-x}Ni_xO_4$ will introduce less magnetization in the doped system. Furthermore, atom-resolved magnetic moment (Table 5) shows that the magnetic moment of Co and Fe atoms remains almost constant at about 2.8 μ_B and 4.0 μ_B in the doped and undoped systems. In addition, it is observed that the local magnetic moment on the Fe atoms in the tetrahedral site is antiparallel to those of the Fe atoms in the octahedral site. Thus, although in all the compounds (doped and undoped $CoFe_2O_4$), the bulk of the magnetic moment resides on the Fe atoms, their overall contribution to the total magnetic moment is insignificant since the magnetic moment of the Fe atoms at the tetrahedral and octahedral sites cancels out each other. Therefore, the Co and Ni atoms are the main contributors to the overall total magnetic moment per formula unit of the inverse spinel $Co_{1-x}Ni_xFe_2O_4$. In addition, one may expect that with increasing Ni dopant concentration, the total magnetic moment may decrease significantly and tend towards a superparamagnetic state.

4. Conclusion

The microstructural and magneto-optical properties of $Co_{1-x}Ni_xFe_2O_4$ ($0 \leq x \leq 0.6$) prepared by the sol-gel method suitable for magnetic moderate hyperthermia application has been explored in this work. The $Co_{1-x}Ni_xFe_2O_4$ formulated was analyzed using various characterized techniques. The XRD analysis shows that all the samples exhibited a cubic spinel ferrite phase structure. The SEM analysis of the sample revealed a cubic morphology with grain size in the range of 15–100 nm; which decreases with respect to the concentration of Ni to a suitable size for moderate hyperthermia applications. The obtained energy bandgap ranges from 1.52 to 1.55 eV for the various cobalt ferrite compositions. The optical phonon distribution predicted by Raman spectra ranges from 201 to 680 cm^{-1}. The VSM study revealed a ferrimagnetic behavior for all the samples, shifting towards superparamagnetic as the Ni concentration increases. The saturation magnetization and the coercivity also decrease as the Ni atom concentration increases. The self-heating analysis of the formulated $Co_{1-x}Ni_xFe_2O_4$ nanoparticles within the therapeutic range heightens their magnetic hyperthermia application. As the concentration of Ni atom increases, it decreases the heating temperature from 50 °C to 43 °C. Also, the SAR value is reduced from ~28 W/g for the pristine $CoFe_2O_4$ to ~19 W/g at the highest concentration of Ni doping i.e., $Co_{1-x}Ni_xFe_2O_4$ (x = 0.6). This SAR range falls within the therapeutic range and is lower than values obtained in many previous similar studies. The maximum temperature also increases with respect to the magnetic field. It is noteworthy that the synthesized nanoparticles are promising candidates for effective tumoricidal by thermal inducing damage within the therapeutic temperature range. Furthermore, first-principles calculations confirmed the structural, electronic, and magnetic properties of pristine and doped $CoFe_2O_4$ as observed in the experiment. Our work produces pure and nickel-doped cobalt ferrites samples with the requisite properties for an *in vitro* hyperthermia application. Further studies of *in-vivo* application and toxicity tests are being planned and the results will be reported in our future communication.

Credit authors statement

S. O. Aisida: Conceptualization, Data curation, Methodology, Writing – original draft, Software, Reviewing and Editing. **T. C. Chibueze**: Data curation, Visualization, Writing – original draft, Reviewing and Editing **M. H. Alnasir**: Visualization, Data curation, Writing – original draft, Reviewing and Editing **O. E. Oyewande**: Visualization **A. T. Raji**: Visualization, Editing **C. E. Ekuma**: Visualization, Editing, **Ishaq Ahmad**: Visualization, Data curation, **T-k. Zhao**: Visualization, Data curation **M. Maaza**: Visualization, Data curation **F. I. Ezema**: Visualization, Data curation, Investigation.

Declaration of competing interest

Data availability

Data will be made available on request.

Acknowledgments

S. O. Aisida and F. I. Ezema acknowledge TETFUND under the contract number(TETFUND/DR&D/CE/UNI/NSKKA/RP/VOL.1). S. O. Aisida acknowledges the NCP-TWAS Postdoc Fellowship award (NCP-CAAD/TWAS_Fellow8408) and expresses his appreciation to Prof. I. Ahmad, the director of the Experimental Physics lab., National Center for Physics, Islamabad, Pakistan and Prof. F. I. Ezema, Department of Physics and Astronomy University of Nigeria, for their assistance to access some characterization machines for the success of this work. FIE acknowledges the support received from the Africa Centre of Excellence for sustainable Power and Energy Development (ACE-SPED), University of Nigeria, Nsukka.

The authors acknowledge the Center for High Performance Computing (CHPC) in South Africa (https://www.chpc.ac.za/) for the computing hours (i.e., Project MATS0988) made available for the computational aspects of this study.

CEE acknowledges the support from National Science Foundation award No. DMR-2202101. TCC, FIE, and CEE acknowledge the support of the Carnegie Melon Carnegie African Diaspora Fellowship Program. Supercomputer and computational resources were provided by the Lehigh University (LU) High-Performance Computing Center.

References

[1] A.J. Giustini, A.P. Alicia, M.C. Shiraz, A.T. Jennifer, I. Baker, P.H. Jack, Magnetic nanoparticle hyperthermia in cancer treatment, Nano LIFE 1 (2010) 17–32.

[2] M. Sandeep, K. Neeraj, S. Balasubramanian, S. DasappanNair, Citric acid coated CoFe2O4 nanoparticles transformed through rapid mechanochemical ligand exchange for efficient magnetic hyperthermia applications, J. Magn. Magn Mater. 477 (2019) 388–395.

[3] C. Zhang, D.T. Johnson, C.S. Brazel, Numerical study on the multiregion bio-heat equation to model magnetic fluid hyperthermia (MFH) using low Curie temperature nanoparticles, IEEE Trans. Nanobiosci. 7 (4) (2008) 267–275.

[4] D.L. Feldheim, A. Colby, J. Foss, Metal Nanoparticles: Synthesis, Characterization, and Apllications, Marcel Dekker inc., New York, 2002.

[5] J.K. Lim, S.A. Majetich, Composite magnetic-plasmonic nanoparticles for biomedicine, Nano Today 8 (2013) 98–113.

[6] A. Diallo, T. Doyle, B. Mothudi, E. Manikandan, V. Rajendran, M. Maaza, Magnetic behavior of biosynthesized Co3O4 nanoparticles, J. Magn. Magn Mater. 424 (2017) 251–255.

[7] K.T. Arul, E. Manikandan, R. Ladchumananandasivam, M. Maaza, Novel polyvinyl alcohol polymer based nanostructure with ferrites co-doped with nickel and cobalt ions for magneto-sensor application, Polym. Int. 65 (12) (2016) 1482–1485.

[8] L. Monrudee, G. Ranjan, I.K. Puri, Parametric investigation of heating due to magnetic fluid hyperthermia in a tumor with blood perfusion, J. Magn. Magn Mater. 323 (2011) 708–716.

[9] U. Evrim, C. Mustafa, P. Francesco, B. Debora, G. Hakan, Nickel ferrite nanoparticles for simultaneous use in magnetic resonance imaging and magnetic fluid hyperthermia, J. Colloid Interface Sci. 550 (2019) 199–209.

[10] U. Evrim, M. Coşkun, F. Pineider, D. Berti, H. Güngüneş, Nickel ferrite nanoparticles for simultaneous use in magnetic resonance imaging and magnetic fluid hyperthermia, J. Colloid Interface Sci. 550 (2019) 199–209.

[11] S.V. Jadhav, P.S. Shewale, B.C. Shin, M.P. Patil, G.D. Kim, A.A. Rokade, S.S. Park, R.A. Bohara, Y.S. Yu, Study of structural and magnetic properties and heat induction of gadolinium-substituted manganese zinc ferrite nanoparticles for in vitro magnetic fluid hyperthermia, J. Colloid Interface Sci. 541 (2019) 192–203.

[12] A.H. Shah, B. Ahamed, E. Manikandan, R. Chandramohan, M. Iydroose, Magnetic, optical and structural studies on Ag doped ZnO nanoparticles, J. Mater. Sci. Mater. Electron. 24 (7) (2013) 2302–2308.

[13] A. Shah, E. Manikandan, M.B. Ahamed, D.A. Mir, S.A. Mir, Antibacterial and Blue shift investigations in sol–gel synthesized CrxZn1−xO Nanostructures, J. Lumin. 145 (2014) 944–950.

[14] C. Sasikala, N. Durairaj, I. Baskaran, B. Sathyaseelan, M. Henini, E. Manikandan, Transition metal titanium (Ti) doped LaFeO3 nanoparticles for enhanced optical structural and magnetic properties, J. Alloys Compd. 712 (2017) 870–877.

[15] S.O. Aisida, M.H. Alnasir, S. Botha, A. ashir, R. Bucher, I. Ahmad, T.-k. Zhao, M. Maaza, F.I. Ezema, The role of polyethylene glycol on the microstructural, magnetic and specific absorption rate in thermoablation properties of Mn-Zn ferrite nanoparticles by sol-gel protocol, Eur. Polym. J. 132 (2020), 109739.

[16] W. Guangshuo, Z. Fei, L. Xiaoguang, L. Jinlin, M. Yingying, M. Jingbo, Z. Zhixiao, C. Hongwei, Z. Xiaoliang, Controlled synthesis of L-cysteine coated cobalt ferrite nanoparticles for drug delivery, Ceram. Int. 44 (2018) 13588–13594.

[17] A. Fazal, J. Tariq, I. Javed, A. Ishaq, M. Sajjad, H. Naqvic, M. Maaza, Facile synthesis of ferromagnetic Ni doped CeO2nanoparticles withenhanced anticancer activity, Appl. Surf. Sci. 357 (2015) 931–936.

[18] M.N. Madhukara, H.S.N. Bhojya, G. Nagaraju, M. Vinuth, K. Vinu, R. Viswanath, Green synthesis of zinc doped cobalt ferrite nanoparticles: structural, optical, photocatalytic and antibacterial studies, Nano-Struct. Nano-Object 19 (2019), 100322.

[19] N. Madubuonu, S.O. Aisida, A. Ali, I. Ahmad, Z. Ting-kai, S. Botha, M. Maaza, F. I. Ezema, Biosynthesis of iron oxide nanoparticles via a composite of Psidium guavaja-Moringa oleifera and their antibacterial and photocatalytic study, J. Photochem. Photobiol. B Biol. 199 (2019), 111601.

[20] S.O. Aisida, A. Batool, F.M. Khan, L. Rahman, A. Mahmood, I. Ahmad, T.-k. Zhao, M. Maaza, F.I. Ezema, Calcination induced PEG-Ni-ZnO nanorod composite and its biomedical applications, Mater. Chem. Phys. 255 (2020), 123603.

[21] A. Mahnaz, E. Khalil, S.-N. Masoud, Magnetically retrievable ferrite nanoparticles in the catalysis application, Adv. Colloid Interface Sci. 271 (2019), 101982.

[22] T. Chien-Yie, C. Yi-Chun, T. Yung-Kuan, Investigation on structural, magnetic, and FMR properties for hydrothermally-synthesized magnesium-zinc ferrite nanoparticles, Phys. B Condens. Matter 570 (2019) 29–34.

[23] M. Johannsen, U. Gneveckow, L. Eckelt, A. Feussner, N. Waldofner, R. Scholz, S. Deger, P. Wust, S.A. Loening, A. Jordan, Clinical hyperthermia of prostate cancer using magnetic nanoparticles: presentation of a new interstitial technique, Int. J. Hyperther. 21 (2005) 637–647.

[24] S.O. Aisida, A. Ali, O.E. Oyewande, I. Ahmad, A. Ul-Hamid, T.-k. Zhao, M. Maaza, F.I. Ezema, Biogenic synthesis enhanced structural, morphological, magnetic and optical properties of zinc ferrite nanoparticles for moderate hyperthermia applications, J. Nano Res. 23 (2021) 47.

[25] L. De León Prado, D. Cortés Hernández, J. Escobedo Bocardo, G. Hurtado López, Influence of the heat treatment conditions on the properties of gallium-strontium-substituted manganese ferrites designed for magnetic hyperthermia applications, Ceram. Int. 47 (2021) 7069–7080.

[26] P.H. Nam, N.X. Phuc, D.H. Manh, D.K. Tung, V.Q. Nguyen, N.H. Nam, P.K. Son, T. N. Bach, P.T. Phong, Physical characterization and heating efficacy of chitosan-coated cobalt ferrite nanoparticles for hyperthermia application, Phys. E Low-dimens. Syst. Nanostruct. 134 (2021), 114862.

[27] S. Nasrin, F.-U.-Z. Chowdhury, S. Hoque, Study of hyperthermia temperature of manganese-substituted cobalt nano ferrites prepared by chemical co-precipitation method for biomedical application, J. Magn. Magn Mater. 479 (2019) 126–134.

[28] C. Gómez-Polo, V. Recarte, L. Cervera, J. Beato-López, J. López-García, J. A. Rodríguez-Velamazán, M. Ugarte, E.C. Mendonça, J. Duque, Tailoring the structural and magnetic properties of Co-Zn nanosized ferrites for hyperthermia applications, J. Magn. Magn Mater. 465 (2018) 211–219.

[29] M.-B. Carlos, S. Konstantinos, M. Antonios, A. Makis, I. Oscar, G. Pablo, C. Andreu, Y. Lluis, E. Sonia, P. Francesca, Learning from nature to improve the heat generation of iron-oxide nanoparticles for magnetic hyperthermia applications, Sci. Rep. 3 (2013) 1652.

[30] H. Cuizhu, Q. Song, W. Xinzhen, L. Jiurong, L. Liqiang, L. Wei, I. Masahiro, K. Machida, Facile synthesis of hollow porous cobalt spheres and their enhanced electromagnetic properties, J. Mater. Chem. 22 (2012) 22160–22166.

[31] I.d.M. Fernandes, A.L. Lopes-Moriyama, C.P. de Souza, Effect of synthesis parameters on the size of cobalt ferrite crystallite, Ceram. Int. 43 (2017) 3962–3969.

[32] S. Jauhar, J. Kaur, A. Goyal, S. Singhal, Tuning the properties of cobalt ferrite: a road towards diverse applications, RSC Adv. 6 (2016) 97694–97719.

[33] F. Grasset, N. Labhsetwar, D. Li, D. Park, N. Saito, H. Haneda, O. Cador, T. Roisnel, S. Mornet, E. Duguet, J. Portier, J. Etourneau, Langmuir 18 (2002) 8209.

[34] A. Samavati, A.F. Ismail, Antibacterial properties of copper-substituted cobalt ferrite nanoparticles synthesized by co-precipitation method, Particuology 30 (2017) 158–163.

[35] Z. Katerina, R. Vicente, T. Martin, C.-Z. Zara, K. Boris, T. Raquel, M. Ivan, M. Maria, Preparation, characterization and application of nanosized copper ferrite photocatalysts for dye degradation under UV irradiation, Mater. Chem. Phys. 160 (2015) 271–278.

[36] G.N. Mahmoud, M.K. Halimah, D. Arash, K. Ahmad, B.S. Elias, Y.M. Burhanuddin, A comprehensive overview of the structure and comparison of magnetic properties of nanocrystalline synthesized by a thermal treatment method, J. Phys. Chem. Solid. 75 (2014) 315–327.

[37] E. Manikandan, M.K. Moodley, S.S. Ray, B.K. Panigrahi, R. Krishnan, N. Padhy, K. G.M. Nair, A.K. Tyagi, Zinc oxide epitaxial thin film deposited over carbon on various substrate by pulsed laser deposition technique, J. Nanosci. Nanotechnol. 10 (9) (2010) 5602–5611.

[38] W.Y. Lucas, M. Ji-Won, J.R. Claudia, J.L. Lonnie, J.R. Adam, R.T. James, C. C. Bryan, J.P. Tommy, Magnetic properties of bio-synthesized zinc ferrite nanoparticles, J. Magn. Magn Mater. 323 (2011) 3043–3048.

[39] Y. Dong, H. Zhao, Y. Liu, X. Wu, J. Pei, Shape-controlled sysnthesis of colbalt particles by a surfactant-free solvothermal method and their catalytic applications to the thermal decomposition of ammonium perchlorate, CrystEngComm 17 (2015) 9062–9069.

[40] S.O. Aisida, P.A. Akpa, I. Ahmad, T. Zhao, M. Maaza, F.I. Ezema, Bio-inspired Encapsulation and Functionalization of Iron Oxide Nanoparticles for Biomedical Applications, European polymer journal, 2019.

[41] S.H. Wei, L.G. Ferreira, J.E. Bernard, A. Zunger, Electronic properties of random alloys: special quasirandom structures, Phys. Rev. B 42 (15) (1990) 9622.

[42] A. Van De Walle, Multicomponent multisublattice alloys, nonconfigurational entropy and other additions to the Alloy Theoretic Automated Toolkit, Calphad 33 (2) (2009) 266–278.

[43] P. Hohenberg, W. Kohn, Inhomogeneous electron gas, Phys. Rev. 136 (1964) B864–B871.

[44] W. Kohn, L.J. Sham, Self-consistent equations including exchange and correlation effects, Phys. Rev. 140 (1965) A1133–A1138.

[45] J. Perdew, K. Burke, M. Ernzerhof, Generalized gradient approximation made simple, Phys. Rev. Lett. 77 (1996) 3865–3868.

[46] P. Giannozzi, S. Baroni, N. Bonini, M. Calandra, R. Car, C. Cavazzoni, A. Dal Corso, Quantum espresso: a modular and open-source software project for quantum simulations of materials, J. Phys. Condens. Matter 21 (39) (2009), 39550.

[47] D.R. Hamann, M. Schlüter, C. Chiang, Norm-conserving pseudopotentials, Phys. Rev. Lett. 43 (20) (1979) 1494.

[48] D.R. Hamann, Optimized norm-conserving Vanderbilt pseudopotentials, Phys. Rev. B 88 (8) (2013), 085117.

[49] M.J. Van Setten, M. Giantomassi, E. Bousquet, M.J. Verstraete, D.R. Hamann, X. Gonze, G.M. Rignanese, The PseudoDojo: training and grading a 85 element optimized norm-conserving pseudopotential table, Comput. Phys. Commun. 226 (2018) 39–54.

[50] H. Monkhorst, J.D. Pack, Special points for Brillouin-zone integrations, Phys. Rev. B 13 (1976) 5188–5192.

[51] S.L. Dudarev, G.A. Botton, S.Y. Savrasov, C.J. Humphreys, A.P. Sutton, Electron-energy-loss spectra and the structural stability of nickel oxide: an LSDA+ U study, Phys. Rev. B 57 (1998) 1505–1509.

[52] R. Islam, S.D. Molongnenla, J.P. Borah, First principle investigation of the electronic structure of spinel Fe3O4, AIP Conf. Proc. 2115 (2019), 030348.

[53] S. Selcuk, A. Selloni, DFT+ U study of the surface structure and stability of Co3O4 (110): dependence on U, J. Phys. Chem. C 119 (18) (2015) 9973–9979.

[54] M. Cococcioni, S. De Gironcoli, Linear response approach to the calculation of the effective interaction parameters in the LDA+ U method, Phys. Rev. B 71 (3) (2005), 035105.

[55] B. Wang, G. Wang, Z. Lv, WangH, In situ synthesis of hierarchical CoFe2O4 nanoclusters/graphene aerogels and their high performance for lithium-ion batteries, Phys. Chem. Chem. 17 (2015), 27109.

[56] B. Cullity, Element of X-Ray Diffraction, second ed. ed., Addison-Wesley, London, 1978, p. 102.

[57] P.S.V. Mocherla, C. Karthik, R. Ubic, M.S.R. Rao, C. Sudakar, Effect of microstrain on the magnetic properties of BiFeO3 nanoparticles, Appl. Phys. Lett. 105 (2014), 132409.

[58] W. Unchista, M. Santi, S. Ekaphan, EXAFS analysis of cations distribution in structure of Co1−xNixFe2O4 nanoparticles obtained by hydrothermal method in aloe vera extract solution, Appl. Surf. Sci. 380 (2016) 60–66.

[59] K. Hüseyin, B. Abdülhadi, S.T. Muhammet, K. Yüksel, S. Murat, A. Bekir, Cation distribution and magnetic properties of Zn doped NiFe2O4 nanoparticles synthesized by PEG-assisted hydrothermal route, J. Alloys Compd. 479 (2009) 49–55.

[60] J.A. Khan, M. Qasim, B.R. Singh, S. Singh, M. Shoeb, W. Khan, D. Das, A.H. Naqvi, Synthesis and characterization of structural, optical, thermal and dielectric properties of polyaniline/CoFe2O4 nanocomposites with special reference to photocatalytic activity, Spectrochim. Acta Part A: Molecular and Biomolecular 109 (2013) 313–321.

[61] E.S. Sagar, S. Patange, R. Kadam, M. Mane, K. Jadhav, Structure refinement, cation site location, spectral and elastic properties of Zn2+ substituted NiFe2O4, J. Mol. Struct. 1024 (2012) 77–83.

[62] T.R. Tatarchuk, N.D. Paliychuk, M. Bououdina, B. Al-Najar, M. Pacia, W. Macyk, A. Shyichuk, Effect of cobalt substitution on structural, elastic, magnetic and optical properties of zinc ferrite nanoparticles, J. Alloys Compd. 731 (2018) 1256–1266.

[63] J.D. Baraliya, H.H. Joshi, Spectroscopy investigation of nanometric cobalt ferrite synthesized by different techniques, Vib. Spectrosc. 74 (2014) 75–80.

[64] P. Chandramohan, Srinivasan, Velmurugan, Narasimhan, Cation distribution and particle size effect on Raman spectrum of CoFe2O4, J. Solid State Chem. 184 (2011) 89–96.

[65] T. Yu, Shen, Y. Shi, J. Ding, Cation migration and magnetic ordering in spinel CoFe2O4 powder: micro-Raman scattering study, J. Phys. Condens. Matter 14 (2002) L613.

[66] S. Raghvendra, K. Ivo, V. Jarmila, H. Jaromir, M. Jiri, K. Lukas, T. Jakub, Š. Jiří, E. Vojtěch, H. Miroslava, Impact of grain size and structural changes on magnetic, dielectric, electrical, impedance and modulus spectroscopic characteristics of CoFe$_2$O$_4$ nanoparticles synthesized by honey mediated sol-gel combustion method, Adv. Nat. Sci. Nanosci. Nanotechnol. 8 (2017), 045002.

[67] M. Chithra, C.N. Anumol, S. Baidyanath, C.S. Subasa, Structural and magnetic properties of Zn$_X$Co$_{1-X}$Fe$_2$O$_4$ nanoparticles:Nonsaturation of magnetization, J. Magn. Magn Mater. 424 (2017) 174–184.

[68] R. Kambale, P. Shaikh, S. Kamble, Y. Kolekar, Effect of cobalt substitution on structural, magnetic and electric properties of nickel ferrite, J. Alloys Compd. 478 (2009) 599–603.

[69] K.R. Srinivasa, P.R. Appa, M.V. Chaitanya, K.H. Rao, Development of Least Sized Magnetic Nanoparticles with High Saturation Magnetization, vol. 750, 2018, pp. 838–847.

[70] V.W. Grant, K. John, P.M. Peter, R. Sergey, V.C. Shen, The effect of different Fe concentrations on the structural and magnetic properties of near-surface superparamagnetic Ni1− xFex nanoparticles in SiO$_2$ made by dual low energy, J. Magn. Magn Mater. 473 (2018) 125–130.

[71] S.O. Aisida, P.A. Akpa, I. Ahmad, M. Maaza, F.I. Ezema, Influence of PVA, PVP and PEG doping on the optical, structural, morphological and magnetic properties of zinc ferrite nanoparticles produced by thermal method, Phys. B Condens. Matter 571 (2019) 130–136.

[72] B. Patrick, Magnetic surface anisotropy of cobalt and surface roughness effects within Neel's model, J. Phys. F Met. Phys. 18 (1988) 1291–1298.

[73] S. Gore, R. Mane, Naushad, S. Jadhav, M. Zate, Z. Alothman, B. Hui, Influence of Bi^{3+}-doping on the magnetic and Mössbauer properties of spinel cobalt ferrite, Dalton Trans. 44 (2015) 6384.

[74] G. Muscas, N. Yaacoub, G. Concas, F. Sayed, R.H. Sayed, J.M. Greneche, C. Cannas, A. Musinu, V. Foglietti, S. Casciardi, C. Sangregorio, D. Peddis, Evolution of the magnetic structure with chemical composition in spinel iron oxide nanoparticles, Nanoscale 7 (2015) 13576–13585.

[75] K. Kombaiah, J.V. Judith, L.K. John, M. Bououdina, A.A.-L. Hamad, R.R. Jothi, Studies on Opuntia dilenii haw mediated multifunctional ZnFe$_2$O$_4$ nanoparticles: optical, magnetic and catalytic, Mater. Chem. Phys. 194 (2017) 153–164.

[76] H. Abdallah, T. Moyo, Nagema, The effect of temperature on the structure and magnetic properties of Co$_{0.5}$Ni$_{0.5}$Fe$_2$O$_4$ spinel nanoferrite, J. Magn. Magn Mater. 394 (2015) 223–228.

[77] G.R. Iglesias, Y. Jabalera, A. Peigneux, B.L.C. Fernández, Á.V. Delgado, C. Jimenez-Lopez, Enhancement of magnetic hyperthermia by mixing synthetic inorganic and biomimetic magnetic nanoparticles, Pharmaceutics 11 (2019) 273.

[78] Y. Jabalera, A. Sola-Leyva, S.C. Gaglio, M.P. Carrasco-Jiménez, G.R. Iglesias, M. Perduca, C. Jimenez-Lopez, Enhanced cytotoxic effect of TAT–PLGA-embedded DOXO carried by biomimetic magnetic nanoparticles upon combination with magnetic hyperthermia and photothermia, Pharmaceutics 13 (2021) 1168.

[79] P.R. Appa, K.R. Srinivasa, T.R. Pydi, K. Govinda, C. Mounika, M.V. Chaitanya, K. Rao, A systematic study of cobalt-zinc ferrite nanoparticles for self regulated magnetic hyperthermia, J. Alloys Compd. 794 (2019) 60–67.

[80] Y. Jabalera, A. Sola-Leyva, A. Peigneux, F. Vurro, G.R. Iglesias, J. Vilchez-Garcia, I. Pérez-Prieto, F.J. Aguilar-Troyano, L.C. López-Cara, M.P. Carrasco-Jiménez, C. Jimenez-Lopez, Biomimetic magnetic nanocarriers drive choline kinase alpha inhibitor inside cancer cells for combined chemo-hyperthermia therapy, Pharmaceutics 11 (2019) 408.

[81] P. Rodriguez, D. Hernandez, J. Bocardo, J. Robles, H. Fuentes, A. Teran, L. Prado, J. Nonell, G. Lopez, Structural and magnetic properties of Mg-Zn ferrites (Mg1−xZnxFe2O4) prepared by sol-gel method, J. Magn. Magn Mater. 427 (2017) 268–271.

[82] F. Reyes-Ortega, Á.V. Delgado, E.K. Schneider, B.L.C. Fernández, G.R. Iglesias, Magnetic nanoparticles coated with a thermosensitive polymer with hyperthermia properties, Polymers 10 (2018) 10.

[83] C.E. Arinzechukwu, S.O. Aisida, A. Agbogu, I. Ahmad, F.I. Ezema, Polyethylene glycol capped nickel–zinc ferrite nanocomposites: structural, optical and magnetic properties suitable for hyperthermia applications, Appl. Phys. A 128 (2022) 1088.

[84] W. Leea, S. Bae, Y. Takemura, I.B. Shim, T.M. Kim, J. Kim, H. Lee, S. Zurn, C. Kim, Self-heating characteristics of cobalt ferrite nanoparticles for hyperthermia application, J. Magn. Magn Mater. 310 (2007) 2868–2870.

[85] K. Dong-Hyun, E.N. David, T.J. Duane, S.B. Christopher, Heat generation of aqueously dispersed CoFe2O4 nanoparticles as heating agents for magnetically activated drug delivery and hyperthermia, J. Magn. Magn Mater. 320 (2008) 2390–2396.

[86] E.A. Deatsch, B.A. Evans, Heating efficiency in magnetic nanoparticle hyperthermia, J. Magn. Magn Mater. 354 (2014) 163–172.

[87] K. Kombaiah, J.J. Vijaya, L.J. Kennedy, M. Bououdina, B. Al-Najar, Conventional and microwave combustion synthesis of optomagnetic CuFe2O4 nanoparticles for hyperthermia studies, J. Phys. Chem. Solid. 115 (2017) 162–171.

[88] Z. Boekelheide, Z.A. Hussein, S.M. Harstad, A.A. El-Gendy, R.L. Hadimani, Gd 5 Si 4 micro-and nano-particles for self-regulated magnetic hyperthermia, IEEE Trans. Magn. 53 (2017) 1–4.

[89] M.H. Alnasir, M.Y. Khan, W.B. Ali, M.Z. Ansar, S. Manzoor, Magnetic and hyperthermia properties of Ni1− xCux nanoparticles coated with oleic acid and silica prepared via sol–gel method, Appl. Phys. A 125 (2019) 532.

[90] S. Matsuda, T.K. Kisako, T. Osaka, Synthesis of cobalt ferrite nanoparticles using spermine and their effect on death in human breast cancer cells under an alternating magnetic field, Electrochim. Acta 183 (2015) 153–159.

[91] H.M. El-Sayed, I.A. Ali, A. Azzam, A.A. Sattar, Influence of the magnetic dead layer thickness of Mg-Zn ferrite nanoparticle on their magnetic properties, J. Magn. Magn Mater. 424 (2017) 226–232.

[92] A. Doaga, A.M. Cojocariu, W. Amin, F. Heib, P. Bender, R. Hempelmann, O. F. Culton, Synthesis and characterizations of manganese ferrites for hyperthermia applications, Mater. Chem. Phys. 143 (2013) 305–310.

[93] E.L. Verde, G.T. Landi, J.d.A. Gomes, M.H. Sousa, A.F. Bakuzis, Magnetic hyperthermia investigation of cobalt ferrite nanoparticles: comparison between experiment, linear response theory, and dynamic hysteresis simulations, J. Appl. Phys. 111 (12) (2012), 123902.

[94] J. Carrey, B. Mehdaoui, M. Respaud, Simple models for dynamic hysteresis loop calculations of magnetic single-domain nanoparticles: application to magnetic hyperthermia optimization, J. Appl. Phys. 109 (8) (2011), 083921.

[95] M.R. Barati, C. Selomulya, K.G. Sandeman, K. Suzuki, Extraordinary induction heating effect near the first order Curie transition, Appl. Phys. Lett. 105 (16) (2014), 162412.

[96] B. Olivier, in: R T (Ed.), Science Data Book, 1971.